JOURNAL OF PROPULSION AND POWER
Vol. 21, No. 2, March–April 2005

Computational Analysis of Inlet Aerodynamics for a Hypersonic Research Vehicle

Manoj T. Nair,* Naresh Kumar,† and S. K. Saxena‡
National Aerospace Laboratories, Bangalore 560017, India

The aim of the present work is to carry out Reynolds-averaged Navier–Stokes computations of flow through the inlet of a hypersonic research vehicle with a view to accomplish detailed aerodynamic analysis. Three inlet configurations that differ in the inlet-duct height are considered in this study. The results of this study are presented in the form of detailed computational flow visualization through density contours, variation of flow parameters at various desired sections, and inlet performance in each case.

Nomenclature

C_p	=	pressure coefficient
$\hat{\boldsymbol{E}}$	=	transformed inviscid flux vector $\hat{\boldsymbol{F}}$, $\hat{\boldsymbol{G}}$, or $\hat{\boldsymbol{H}}$ in ξ, η, or ζ directions, respectively
$\hat{\boldsymbol{E}}_v$	=	transformed viscous flux vector $\hat{\boldsymbol{F}}_v$, $\hat{\boldsymbol{G}}_v$, or $\hat{\boldsymbol{H}}_v$ in ξ, η, or ζ directions, respectively
e	=	total energy per unit volume
I	=	internal energy per unit mass
J	=	Jacobian of transformation
L	=	length of the body
M	=	Mach number
Pr	=	Prandtl number
p	=	static pressure
$\boldsymbol{Q}$	=	vector of conserved variables
$\hat{\boldsymbol{Q}}$	=	$\boldsymbol{Q}/J$
Re	=	Reynolds number
t	=	time
u, v, w	=	Cartesian components of fluid velocity
$\boldsymbol{W}$	=	contravariant velocity vector
x, y, z	=	Cartesian coordinates
γ	=	ratio of specific heats
ξ, η, ζ	=	transfomed (computational) coordinates
ρ	=	density

Subscript

∞	=	freestream conditions

Introduction

LOW-COST access to space with reusable vehicles employing airbreathing propulsion will open a new window for future progress of mankind. There are competing efforts from several industrial countries including India to put forward conceptual designs and feasibility studies for a viable technology for this purpose. One such effort is currently in progress at Defence Research and Development Laboratory for the design and development of a hypersonic research vehicle (HRV) that employs airbreathing propulsion. The inlet is a very critical component of such a vehicle and needs to be highly efficient for this technology to succeed. The inlet consists of a forebody and an integrated duct, the initial compression being carried out by the forebody.

The flow through the inlet is characterized by shock-shock interaction, shock-boundary-layer interaction, and development of thick turbulent boundary layers over the forebody, which if allowed to enter the inlet duct can lead to adverse effects on the inlet performance.[1] Although the inlet duct can be two dimensional, the flow approaching the duct entrance can be highly three dimensional. In view of all this, the three-dimensional Reynolds-averaged Navier–Stokes (RANS) equations are the appropriate mathematical model for the analysis of such a flow.

The aim of the present work is to carry out RANS computations of flow through the inlet of a HRV with a view to accomplish detailed aerodynamic analysis. The emphasis is on the mass flow rates and pressure recovery obtained at the entrance of the inlet duct after the ramps. Only a short inlet-duct length after the entrance is considered, and attention is focused on the flow in this region and how this flow is effected when the duct height is varied. An in-house developed RANS code MB-EURANIUM with Spalart–Allmaras model of turbulence[2–6] is employed for this purpose. Three inlet configurations that differ in the inlet-duct height are considered in this study. The results of this study are presented in the form of detailed flow visualization through density contours, variation of flow parameters at various desired sections, and inlet performance in each case.

Governing Flow Equations

The code MB-EURANIUM solves full three-dimensional RANS equations. These equations in generalized body-fitted coordinate system are written as

$$\frac{\partial \hat{\boldsymbol{Q}}}{\partial t} + \frac{\partial \hat{\boldsymbol{F}}}{\partial \xi} + \frac{\partial \hat{\boldsymbol{G}}}{\partial \eta} + \frac{\partial \hat{\boldsymbol{H}}}{\partial \zeta} = \frac{1}{Re}\left\{\frac{\partial \hat{\boldsymbol{F}}_v}{\partial \xi} + \frac{\partial \hat{\boldsymbol{G}}_v}{\partial \eta} + \frac{\partial \hat{\boldsymbol{H}}_v}{\partial \zeta}\right\} \tag{1}$$

where

$$\hat{\boldsymbol{Q}} = \frac{1}{J}\begin{pmatrix} e \\ \rho \\ \rho u \\ \rho v \\ \rho w \end{pmatrix} \qquad \hat{\boldsymbol{E}} = \frac{1}{J}\begin{pmatrix} (e+p)\boldsymbol{W} \\ \rho \boldsymbol{W} \\ \rho u \boldsymbol{W} + p\kappa_x \\ \rho v \boldsymbol{W} + p\kappa_y \\ \rho w \boldsymbol{W} + p\kappa_z \end{pmatrix} \tag{2}$$

Here Re is the freestream Reynolds number based on a characteristic length. The details of the RANS equations in the code MB-EURANIUM are available in Saxena and Nair[5] and Nair et al.[7] The coefficient of molecular viscosity is computed employing Sutherland's law, and a turbulence model is used to obtain the coefficient of eddy viscosity. A perfect gas assumption is made, and the Prandtl number is taken to be equal to 0.9.

Received 6 June 2003; revision received 15 May 2004; accepted for publication 16 May 2004.

*Scientist, Computational and Theoretical Fluid Dynamics Division. Member AIAA.
†Scientist, Computational and Theoretical Fluid Dynamics Division.
‡Senior Scientist, Computational and Theoretical Fluid Dynamics Division. Associate Fellow AIAA.

Numerical Approach

A brief outline of the numerical approach followed to solve the RANS equations is presented here. The code MB-EURANIUM employs a total-variation-diminishing (TVD) formulation of Roe's Riemann solver based on the monotone upwind scheme for conservation laws within the framework of a cell-centered finite volume approach and generalized body-fitted coordinates to discretize the Euler terms.[3] A variety of entropy fixes and TVD limiters are available to suit a problem. The viscous terms are central differenced. The time term is discretized using a multistage Runge–Kutta time-stepping scheme. A number of convergence acceleration techniques have been introduced in the code to enhance its efficiency. These include local time-stepping, upwind implicit residual averaging, grid sequencing, and multigrid techniques. The algebraic Baldwin–Lomax[8] turbulence model and the one-equation Spalart–Allmaras[9] turbulence model are available to simulate turbulent flows.[5] Freestream conditions are specified at the inflow boundary, and extrapolation boundary condition is applied at the outflow boundary. The wall is taken as adiabatic. The multiblock capability allows handling of complex configurations without any difficulty. The code has been parallelized using message-passing-interface libraries and can be ported on any parallel platform having these libraries.

Spalart–Allmaras Turbulence Model

Inspired by the Baldwin–Barth[10] work, Spalart and Allmaras[9] developed a new one-equation model, which was derived from scratch to avoid any ancestry and ensure future growth. The derivation employs certain empiricism and arguments of dimensional analysis, Galilean invariance, and selective dependence on the molecular viscosity. The model is numerically forgiving, in terms of near-wall resolution and stiffness, and yields fairly rapid convergence to steady state. The wall and freestream boundary conditions are trivial. The details of the implementation and limited testing of Spalart–Allmaras (SA) model in the code MB-EURANIUM are available in Saxena and Nair.[5] The turbulent flow computations presented in the present work employ the SA model.

Test Cases

Three different test cases that differ only in inlet-duct height are considered. The inlet-duct heights for the three cases are as follows: 1) inlet A, 220 mm; 2) inlet B, 230 mm; and 3) inlet C, 240 mm. The freestream conditions are provided in Table 1. These conditions correspond to an altitude of 35 km.

Grid Generation

The geometric details of the body are shown in Fig. 1. The x axis was taken along the axis of the body, z axis was taken to be in the span-wise direction and y axis was along the height of the duct. Assuming symmetry along the z direction, only half of the body is taken for computations. The inlet duct (Ref. Fig. 1) has a width of 0.8 m (z direction), and the height varies from 220 to 240 mm for different test cases. The duct is open in the x direction. In the y direction, there are walls on both the sides, and in the z direction there is wall at one end and symmetry plane at the other. A 54-block structured Navier–Stokes grid with a C-O topology and 1.8 million grid points was generated employing GRIDGEN.[11] The grid generation involved the coupling of the internal and the external flow.

Table 1 Freestream conditions

Parameter	Value
Reynolds number Re	5.4×10^6
Freestream Mach number M_∞	6.5
Angle of attack α, deg	7 deg
Freestream temperature T_∞	242.7 K
Freestream pressure P_∞	582.9 N/m^2
Ratio of specific heats γ	1.4
Wall condition	Adiabatic
Prandtl number	0.9

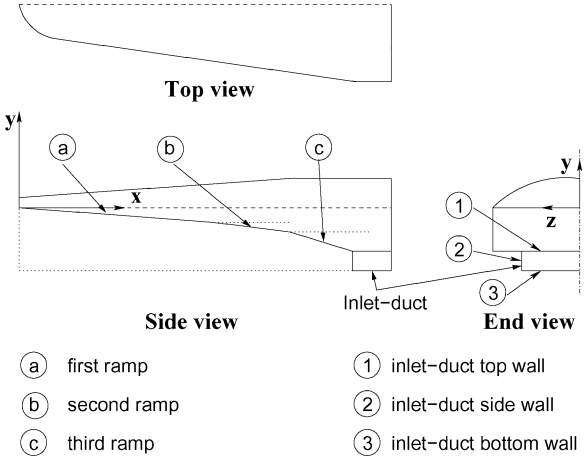

Fig. 1 Nomenclature for the configuration.

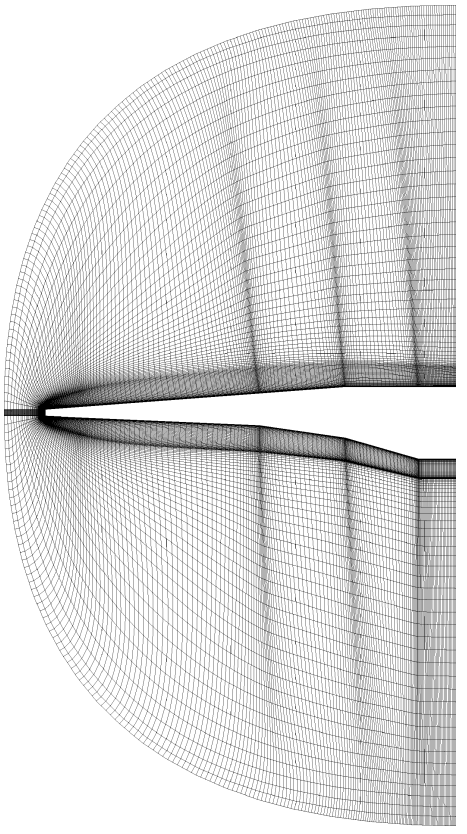

Fig. 2 Pitch-plane grid for the HRV.

Figure 2 shows the pitch-plane grid for the vehicle. Figure 3 shows the sectional view of the grid on the bottom side of the vehicle.

Grid-Independence Study

A limited grid-independence study is conducted for the first test case (inlet A). Two different grids were taken. The first grid (grid A) has 61 points inside the duct along its height (y direction). The second grid (grid B) has 41 points along the height. Figure 4 shows the grid point distribution along the duct height (y direction) for both the grids. Figure 5 shows the C_p variation along the x axis for both the grids; the results are seen to be almost identical. Tables 2 and 3 present the inlet performance parameters for the two grids. The difference in the mass flow rates obtained from the two grids is not significant. This gives some confidence that the boundary layer might have been adequately resolved. The pressure recovery is however seen to be more sensitive to the refinement of the grid. Figure 6 shows the y^+ distribution along the top wall in the z direction at the

Table 2 Performance comparisons for inlet A using grids A and B

	Mass flow rate, kg/s		
Inlet	N-S	Ideal	% capture
Grid A	24.58	33.94	72.43
Grid B	24.74	33.94	72.89

Table 3 Comparison of pressure recovery for inlet A using grids A and B

	Pressure recovery	
Inlet	Duct entrance	Duct exit
Grid A	0.47	0.21
Grid B	0.56	0.28

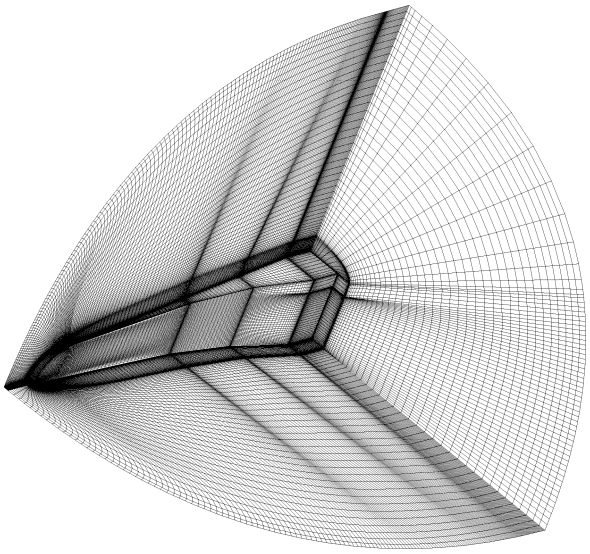

Fig. 3 Sectional view of the grid around the HRV.

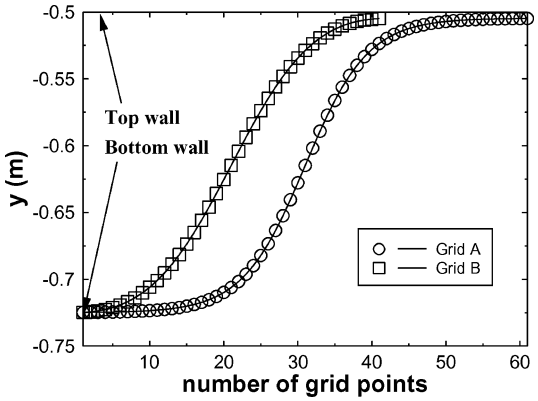

Fig. 4 Grid point distribution in the y direction inside the duct of inlet A.

entrance of the inlet duct for the two grids. The y^+ for the grid A is seen to be less than one, whereas y^+ for grid B appears to be of the order of 5. No further reference to grid A is made in the paper, and all of the results presented next are based on grid B.

Results and Discussions

The test cases studied have three compression ramps to compress the incoming air before it enters the inlet duct. In the first test case (inlet A), the height of the inlet duct is 220 mm. Figure 7a provides the density contours at the pitch plane for the complete inlet for this case. The blunt-body shock is sharply captured. The shocks at the junction of the first and second ramp and the second and third ramp are also clearly visible. These three shocks appear to hit the lip of

Table 4 Mass flow rates at the entrance of the inlet duct for the three inlets

	Mass flow rate, kg/s		
Inlet	N-S	Ideal	% capture
A	24.74	33.94	72.89
B	24.96	34.22	72.98
C	25.96	34.48	75.31

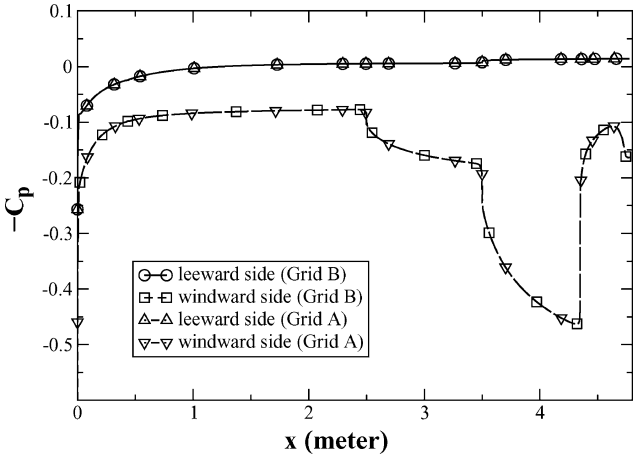

Fig. 5 C_p variation along the x axis at the pitch plane for inlet A.

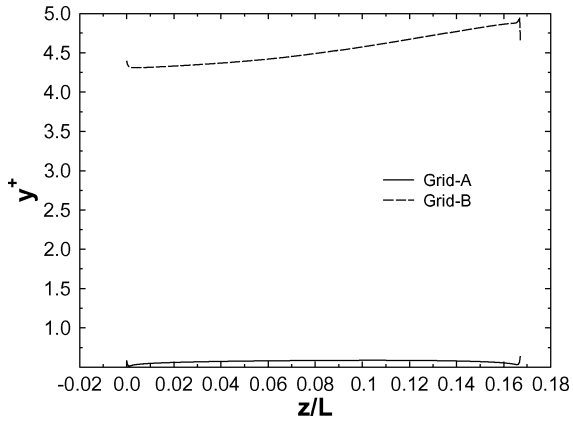

Fig. 6 The y^+ variation along the z axis at the entrance of the inlet duct on the top wall for inlet A.

the inlet duct on the bottom wall. In a blown-up view of the density contours at the rear, shown in Fig. 7b, the reflected shock inside the duct is seen to interact with the incoming boundary layer on the top wall of the duct. An expansion fan emanating from the top-wall leading edge can also be identified interacting with the reflected shock. All of this makes the flow inside the duct quite complex. The external flow on the forebody is equally complex and is characterized by the shock-boundary-layer interaction at the compression corners of the ramps and shock-shock interaction at the lip of the inlet duct.

Density contours at the pitch plane for inlet B and inlet C are presented in Fig. 8 and 9, respectively. In these cases, the compression corner shocks seem to hit inside the duct and not at the lip. As the inlet height increases, the ramp shocks hit deeper inside the duct. The boundary layer entering the inlet has an adverse effect on the performance of the inlet. The ways to mitigate this adverse effect is an important design issue.[1]

The relative performance of the three inlets is compared in Tables 4–6. It can be seen that inlet C provides the best performance, both in terms of mass flow capture and the total pressure recovery. The average Mach numbers at the end of the compression ramps are also provided. The ideal mass flow rate is calculated as the mass flow rate entering an area along the dotted line in Fig. 1 with width equal to the width of the inlet. The difference in the mass flow rates

Table 5 Relative performance of the three inlets

	Pressure recovery	
Inlet	Duct entrance	Duct exit
A	0.56	0.28
B	0.57	0.28
C	0.59	0.29

Table 6 Relative performance of the three inlets.

	Mach number	
Inlet	Duct entrance	Duct exit
A	3.72	3.15
B	3.77	3.18
C	3.91	3.30

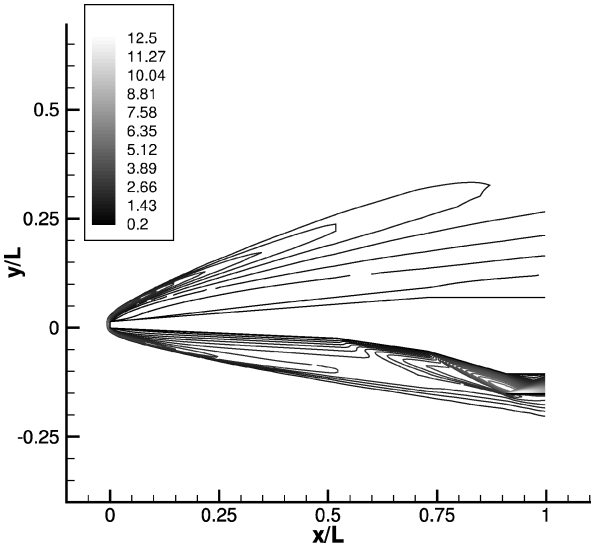

a) Full view

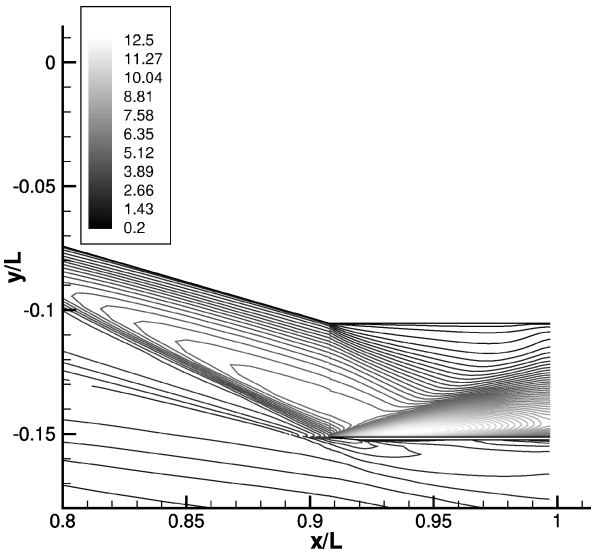

b) Close-up at the inlet duct

Fig. 7 Density contour at the pitch plane of the HRV for inlet A.

between RANS and Euler computations for inlet A is as follows: for Euler, 25.48 kg/s; for RANS, 24.74 kg/s with percentage of 97.09 of Euler. The difference is small, indicating that the viscous effects on the mass flow rate are small at the entrance of the duct.

The C_p at the pitch plane for inlet A is presented in Fig 5. This clearly brings out the large contribution to lift from the forebody.

The variation of pressure at four spanwise sections (constant z) at the entrance of the inlet duct for inlets A and C is given in Fig. 10,

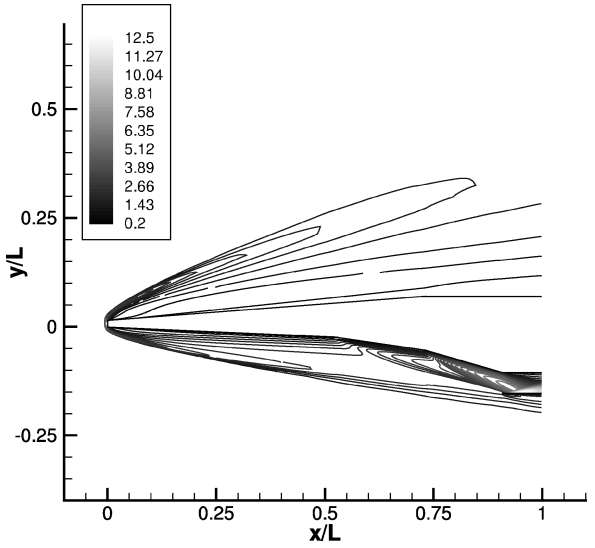

a) Full view

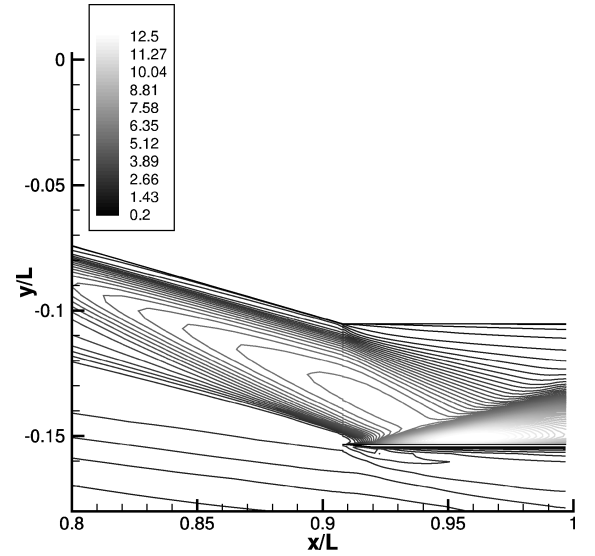

b) Close-up at the inlet duct

Fig. 8 Density contour at the pitch plane of the HRV for inlet B.

whereas the pressure variation along the span at sections along the y coordinate (height of the duct) is provided in Fig. 11. The variation at different z stations indicates that for inlet C the ramp shocks hit much deeper inside compared to inlet A. From both of the figures there is a near constant pressure along the z direction up to $y = -0.65$ m. Beyond that, the pressure drops drastically. In Fig. 10 there is an increase in pressure at the bottom wall. A similar increase in pressure can be noted on the side wall in Fig. 11. This increase in pressure is caused by the presence of oblique shocks from the leading edge of the bottom and side walls, respectively. In Fig. 10 there is a drop in pressure on the top wall of the inlet duct caused by the presence of an expansion fan. A similar distribution for Mach number and density is presented in Figs. 12–15. The variation in Mach number (Fig. 12) shows the presence of the boundary layer on the top surface. The density variation in the Fig. 14 is an indication of the effect of viscosity. Though the pressure at similar locations in Fig. 10 shows near constant behavior for a large part, this is not so for density. The density variations at the duct inlet along the z direction are small up to about $y = -0.65$ (Fig. 11).

The nonuniformity in the profiles, particularly near the lower lip of the inlet duct ($y \approx -0.7$), can be noted in these figures. The variation of the flow properties along the z coordinate is larger for $y = -0.7$ m than those at other y sections shown. This large variation near the lip of the duct can also be noted in the figures showing the variation of properties along the y coordinate for various z sections.

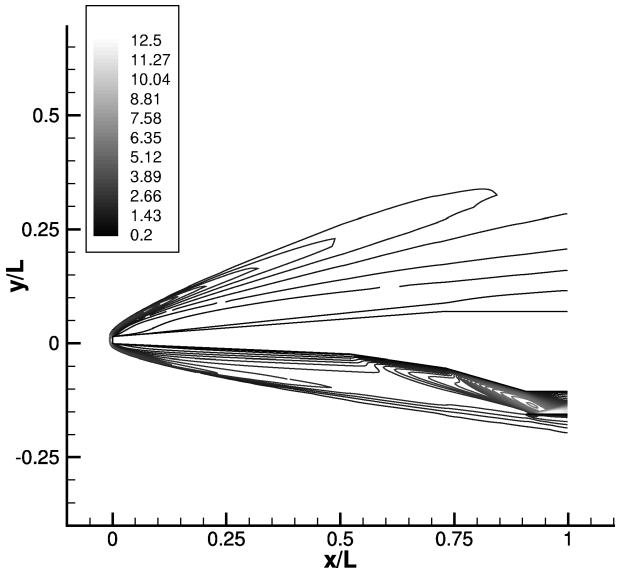

a) Full view

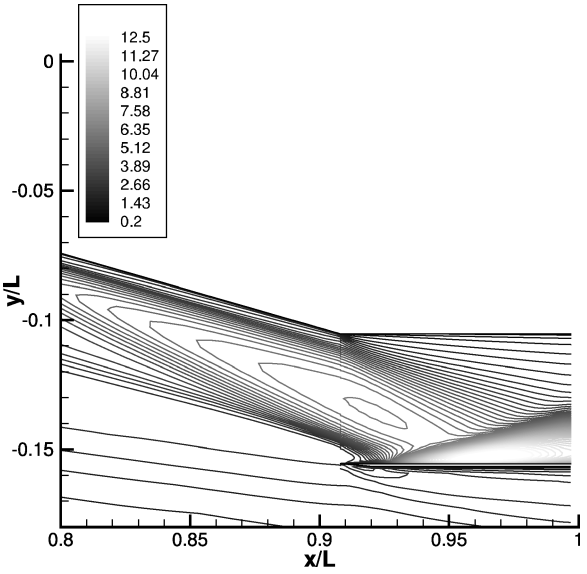

b) Close-up at the inlet duct

Fig. 9 Density contour at the pitch-plane of the HRV for inlet C.

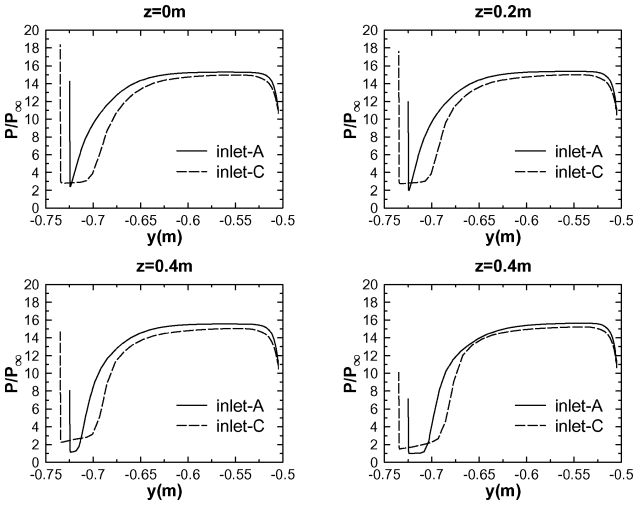

Fig. 10 P/P_∞ variation along the y at different z sections at the entrance of the inlet duct for inlets A and C.

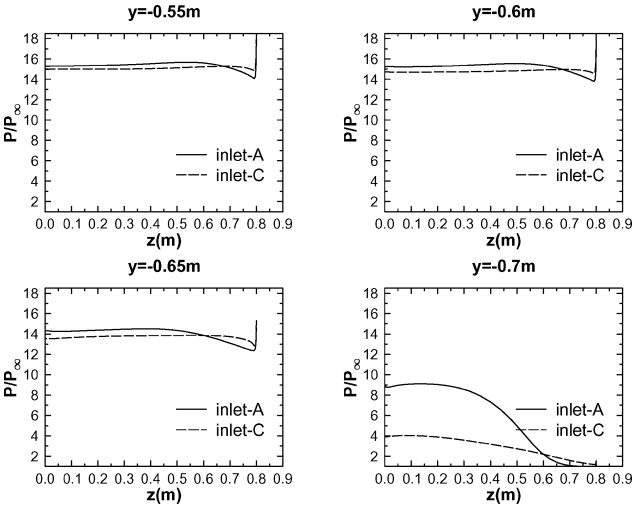

Fig. 11 P/P_∞ variation along the z at different y sections at the entrance of the inlet duct for inlets A and C.

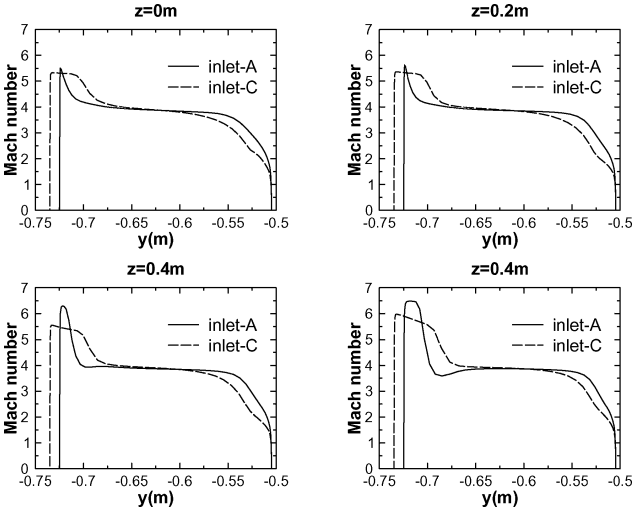

Fig. 12 Mach-number variation along the y at different z sections at the entrance of the inlet duct for inlets A and C.

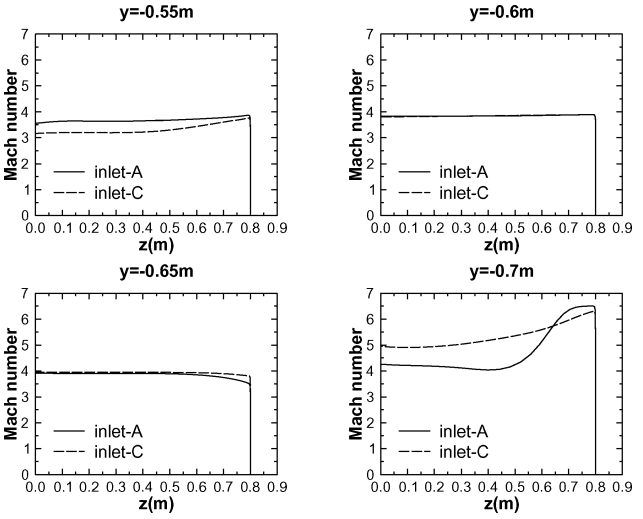

Fig. 13 Mach-number variation along the z at different y sections at the entrance of the inlet duct for inlets A and C.

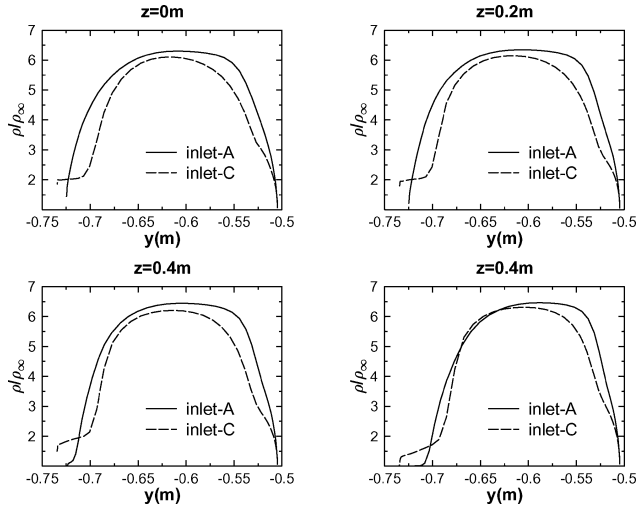

Fig. 14 Density variation along the y at different z sections at the entrance of the inlet duct for inlets A and C.

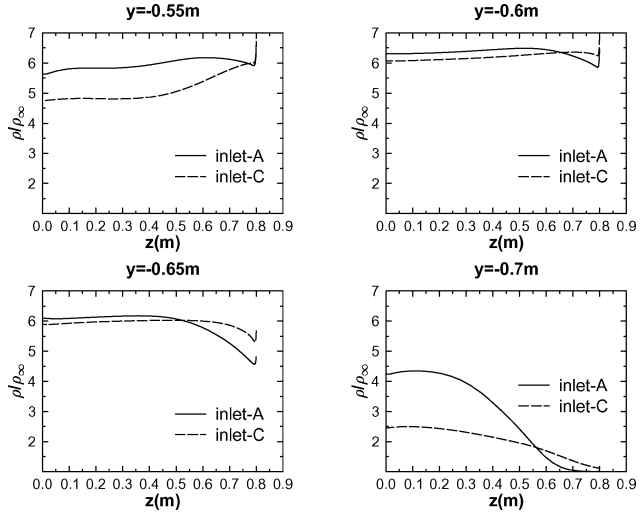

Fig. 15 Density variation along the z at different y sections at the entrance of the inlet duct for inlets A and C.

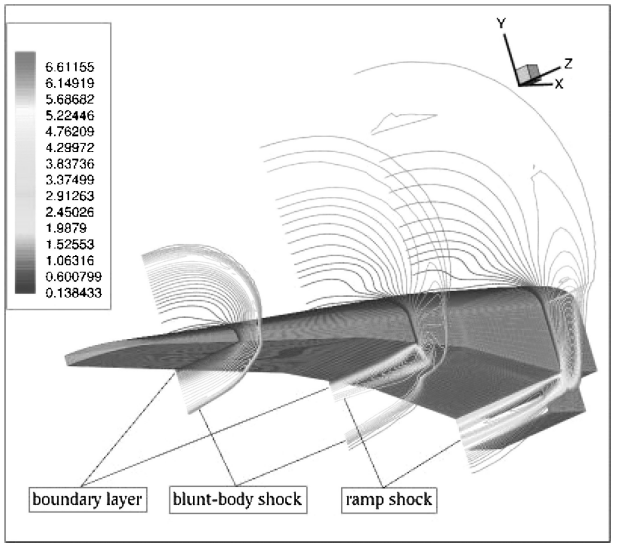

Fig. 16 Density contours at three different sections (x = 1.25, 3.0, and 4.35 m) for inlet C.

The variation of Mach number at the entrance of the inlet duct shown in Figs. 12 and 13 indicates that close to the lip of the inlet duct the Mach numbers could be close to the freestream value. This is more prominent in the case of inlet C. This is caused by the ramp shocks crossing the entrance plane and hitting a deeper inlet duct inside compared to inlet A. It can be inferred from these sectional variations that the viscous effects play a significant role in the flow distortion. This could lead to pressure loss and lower pressure recovery at the entrance of the duct.

Figure 16 shows the density contours at three different sections of the three inlets along the axial direction for the inlet C. All of the flow features just discussed can again be identified here. The important point that comes out of this picture is that the flow approaching the inlet duct is highly three-dimensional and viscous.

Conclusions

A detailed aerodynamic analysis of the inlet of a hypersonic research vehicle has been successfully carried out employing the RANS code MB-EURANIUM with the Spalart–Allmaras model of turbulence. The analysis confirms the highly three-dimensional and viscous nature of the complex flow approaching the inlet duct. The boundary layers developed along the forebody enter the duct and can adversely effect the inlet performance. How to mitigate this adverse effect is an important design issue. Inlet C provides the best performance. Though the duct area increases by 9% for inlet C compared to inlet A, the corresponding increase in mass flow is only 5%. This is caused by the decrease in density in the cowl region for inlet C as the ramp shocks hit inside the cowl. Detailed numerical flow visualization, variation of flow parameters at desired locations, and comparative study of the performance of the three inlets has been provided.

The fast turnaround achieved (work completed in about one month time, including grid generation for the three cases) in the present complex computational-fluid-dynamics study encourages the view that a RANS simulation can now be employed at much earlier stages of a design cycle than what was previously possible. This should lead to shorter design cycles and better aerodynamic design.

Acknowledgment

This study has been carried out in response to a request from Defence Research and Development Laboratories(DRDL) and is monitored by S. Panneerselvam, Technology Director (Aerodynamics), DRDL. The large-scale parallel computing for the present case was carried out using the 18 processors of Flosolver Mk5 at National Aerospace Laboratories and the 12 processors of Origin 3000 system at CSIR Center for Mathematical Modelling and Computer Simulation (C-MMACS), Bangalore.

References

[1]Goonko, Y., and Mazul, I., "Some Factors of Hypersonic Inlet/Airplane Interactions," *Journal of Aircraft*, Vol. 39, No. 1, 2002, pp. 37–50.

[2]Nair, M. T., and Saxena, S. K., "Multi-Block Euler Computations for Complex Configurations," *Computational Fluid Dynamics Journal*, Vol. 11, No. 1, 2002, pp. 64–77.

[3]Nair, M. T., Rampurawala, A. M., and Saxena, S. K., "MB-EURANIUM User's Manual," National Aerospace Lab., Tech. Rept. PD CF 0110, Bangalore, India, Oct. 2001.

[4]Nair, M. T., and Saxena, S. K., "Reynolds Averged Navier–Stokes Computations for a Light Combat Aircraft," National Aerospace Lab., Tech. Rept. NAL PD CF-0204, Bangalore, India, May 2002.

[5]Saxena, S. K., and Nair, M. T., "Implementation and Testing of Spalart–Allmaras Model in a Multi-Block Code," AIAA Paper 2002-0835, 2002.

[6]Saxena, S. K., and Ravi, K., "Some Aspects of Blunt Body Flow Computations with Roe Scheme," *AIAA Journal*, Vol. 33, No. 6, 1995, pp. 1025–1031.

[7]Nair, M. T., Kumar, N., and Saxena, S. K., "Reynolds Averaged Navier–Stokes Based Aerodynamic Analysis of Inlet of a Hypersonic Research Vehicle," AIAA Paper 2003-7067, 2003.

[8]Baldwin, B. S., and Lomax, H., "Thin-Layer Approximation and Algebraic Model for Seperated Flow," AIAA Paper 78-257, 1978.

[9]Spalart, P. R., and Allmaras, S. R., "A One Equation Turbulence Model for Aerodynamic Flows," AIAA Paper 92-0439, 1992.

[10]Baldwin, B. S., and Barth, T. J., "A One Equation Turbulence Transport Model for High Reynolds Number Wall Bounded Flows," NASA Tech. Rept. TM 102847, Aug. 1990.

[11]Pointwise, *Gridgen User Manual*, ver. 13.3, Bedford, TX, 1999.